

Performance of the CHIRON high-resolution Echelle spectrograph

Christian Schwab^{*a}, Julien F. P. Spronck^a, Andrei Tokovinin^b,
Andrew Szymkowiak^a, Matthew Giguere^a, Debra A. Fischer^a
(^aYale University, New Haven, CT, USA; ^bCTIO, La Serena, Chile)

ABSTRACT

CHIRON is a fiber-fed Echelle spectrograph with observing modes for resolutions from 28,000 to 120,000, built primarily for measuring precise radial velocities (RVs). We present the instrument performance as determined during integration and commissioning. We discuss the PSF, the effect of glass inhomogeneity on the cross-dispersion prism, temperature stabilization, stability of the spectrum on the CCD, and detector characteristics. The RV precision is characterized, with an iodine cell or a ThAr lamp as the wavelength reference. Including all losses from the sky to the detector, the overall efficiency is about 6%; the dominant limitation is coupling losses into the fiber due to poor guiding.

Keywords: Spectroscopy, exoplanets, radial velocities, Doppler method, Echelle, fiber-fed spectrograph, iodine cell

1. INTRODUCTION

Precise radial velocity measurements are crucial for discovery and characterization of extra-solar planets. Even small telescopes equipped with stable Echelle spectrometers can make a significant contribution if a substantial number of nights are secured to ensure high cadence in the observing program. Recognizing this, several observatories are developing such instruments [1,2] to complement more ambitious and expensive RV spectrometers like HARPS, PFS, or ESPRESSO [3-5].

The high-resolution optical spectrometer CHIRON is a facility instrument at the CTIO 1.5m telescope in Chile. Wide wavelength coverage (411 to 877 nm) and medium as well as high spectral resolution modes make it suitable for a variety of stellar spectroscopy tasks. The spectrograph was optimized for Doppler observations with the iodine cell technique, to facilitate searches for extrasolar planets. It was designed to achieve excellent stability and efficiency. In this regard, using a fiber feed to couple the spectrograph onto the telescope to take advantage of improved PSF stability compared to a slit coupled instrument was a critical choice. This makes CHIRON one of the few fiber fed spectrographs utilizing an iodine cell. The instrument design is described in [6]. Here we report on the key aspects of its performance.

CHIRON was designed and built in 2010, funded by NSF MRI grant 0923441 to Fischer. It was commissioned in March 2011, replacing the previous fiber-fed Echelle at the 1.5m telescope which operated since 2008. During its first year, CHIRON demonstrated RV precision on the order of 1m/s and was used by a number of science programs. In an effort to further improve the RV precision and efficiency, we implemented several upgrades in January-February 2012: the old Echelle grating was replaced with a higher efficiency R2 Richardson grating and mounted inside a vacuum enclosure; the fiber link was changed from a round fiber to an octagonal fiber; an anti-reflection coating was applied to the prism; the CCD controller was upgraded to the new NOAO Torrent controller; an exposure meter was added to the spectrometer; and the stability of the temperature control of the instrument was improved.

In Section 2 we give a brief overview of the instrument. In Section 3 the performance of its optical system after the upgrade is detailed. The characteristics of the CCD and exposure meter are given in Sect. 4, stabilization of temperature and pressure is covered in Sect. 5, and overall instrument performance is discussed in Sect. 6.



Figure 1: Part of a solar spectrum, taken with the image slicer.

2. INSTRUMENT OVERVIEW

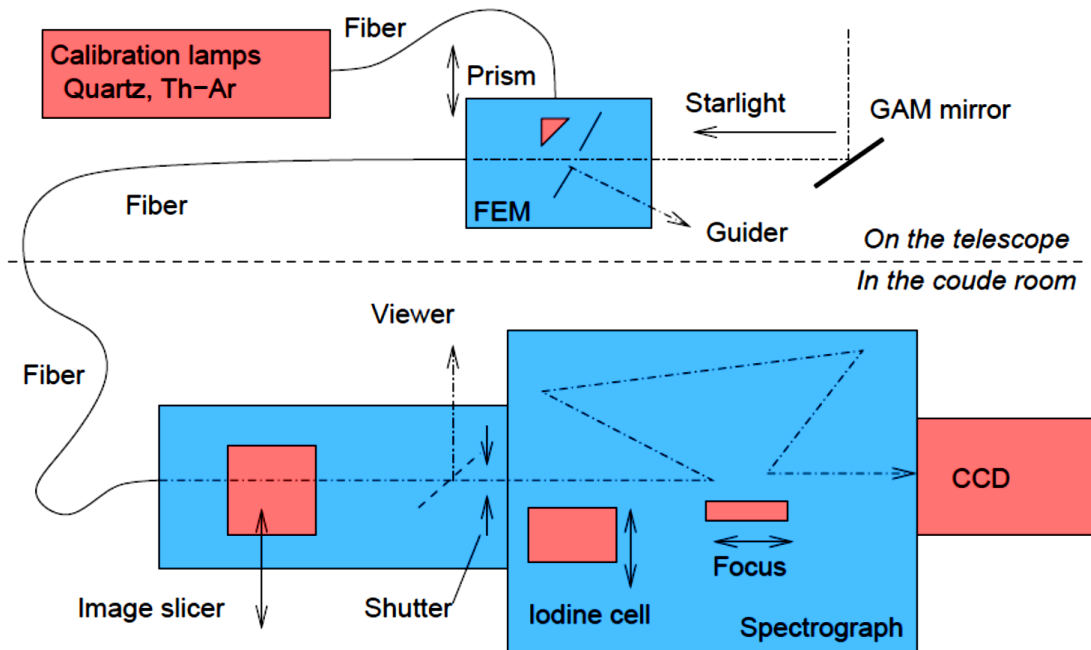


Figure 2: Light path from telescope to detector is shown schematically to illustrate main elements of CHIRON. Pink-colored elements are controlled by the user and the blue elements are fixed.

Figure 2 gives a top-level overview of the CHIRON system. The star light is picked off by a flat mirror attached to the arm of the telescope general-purpose guider. Inside the front-end module (FEM), the star is re-imaged onto the fiber at F/5. The fiber diameter projected on the sky is 2.7 arcseconds; light outside this aperture is used for guiding, based on a small CCD camera CG650 from Prosilica with Gigabit Ethernet interface. The software is an adaptation of the PCguider software used elsewhere at Las Campanas and CTIO; it sends corrections to the telescope tracking motors every second. The light from calibration lamps is fed by another fiber and a tiny prism which is placed behind the entrance aperture by an aero-model servo motor.

The spectrometer is located in the Coude room of the telescope. The light beam emerging from the fiber end is re-imaged by an achromatic doublet into intermediate focus where it can be re-shaped into a slit-like image by the image slicer, to increase spectral resolution with little (~20%) light loss. Figure 2 shows the 2D spectrum with the image slicer. In addition to the slicer, the fiber image can be fed directly to the spectrometer optics (yielding a decreased resolution, $R=28,000$) or intercepted with a slit mask, which increases the resolution with some loss of light. Two more achromats re-collimate the beam with a diameter of 2 mm, and then refocus it with a focal ratio matched to the main collimator (Figure 3). The iodine cell, in a container heated to $+40^{\circ}\text{C}$, can be inserted in the collimated space between the achromats. The main collimator is a 150mm on-axis parabolic mirror; we use a beam diameter of 130mm.

We adopted a pseudo Littrow design with a gamma angle of 6 degrees. The R2 Echelle grating is followed by a single cross dispersing prism, and the spectrum is imaged onto the CCD by a commercial 140mm diameter F/7 amateur telescope, consisting of an oiled triplet front group with a two element field flattener in front of the focal plane. A folding mirror is introduced between the front lens and flattener to save space. The CCD is a LN_2 cooled 4k by 4k chip with $15\ \mu\text{m}$ pixels. The camera triplet is mounted on a translation stage for focusing. About 1% of the light is deflected from the collimated beam to the exposure meter (EM, see below).

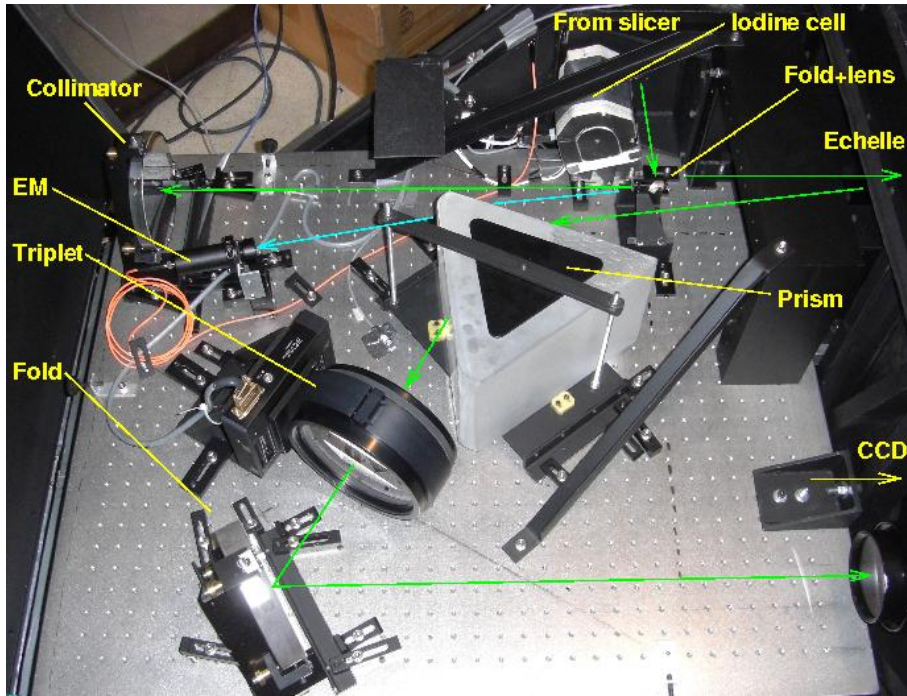


Figure 3: Optical elements of CHIRON. The main light path is shown in green, the EM path in blue (from fold+lens to EM).

3. OPTICAL PERFORMANCE

1.1 Aberrations and PSF

The first light of the instrument is shown in Figure 3, a part of a solar spectrum taken by observing the moon on 21.01.2011. The sodium D lines demonstrate the contrast and resolution CHIRON provides, 120.000 in this configuration. To measure the PSF as function of position on the detector, we recorded the spectrum of a Thorium-Argon (ThAr) lamp using a single mode fiber to feed the spectrograph. The full frame was tiled into 3 x 3 segments. In each segment, all the ThAr lines above a certain threshold that are not blended are averaged to produce a representation of the PSF in this part of the frame. This measurement was done before the upgrade, with the old grating and a slightly larger beam diameter. We expect the aberrations to become slightly less with the new configuration. The result is shown in Figure 4.

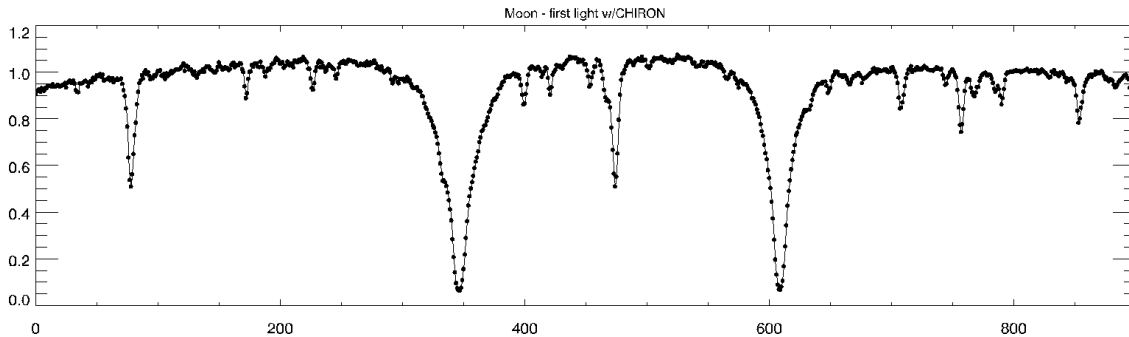


Figure 4: First light of CHIRON, a spectrum of the Moon. This segment shows the Sodium D lines.

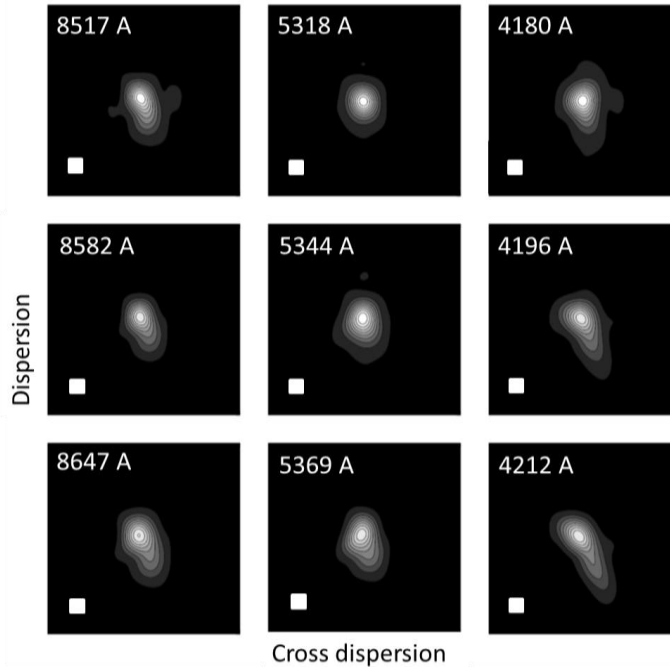


Figure 4: PSF of CHIRON as measured in 9 segments of the CCD. The white square shows the size of 1 pixel.

In particular in the bottom of Figure 4 one can see the effect of aberrations on the PSF. This is at the red end of each order. The largest PSF deformation occurs at the red end of the bluest orders; it has to be noted though that the respective segment of the CCD falls nearly completely out of the FSR of the spectrograph, as the bluest orders only span about half of the width of the chip.

We attribute the majority of the additional wavefront deformations (not inherent to the design) to the glass inhomogeneities of the Schott LF7 prism. It is hard to find glass blocks of suitable size due to the fact that most glasses are melted in strips instead of blocks. An exception is very common glasses like Schott's BK7 and F2 (or the respective equivalents); the latter is a particularly common choice to provide dispersion. We chose a light flint as it provides a slightly more evenly distributed inter-order spacing. The particular block we were able to obtain was old stock, and just large enough to yield a monolithic prism with sufficient clear aperture. Indeed, one corner of the prism was at the edge of the melt, and the refractive index is lower than in the bulk of the material, as can be seen in the interferogram of the prism (Figure 5). To achieve a smooth wavefront over the clear aperture, the surfaces were corrected by hand polishing with a subaperture lap by TORC in Tucson, according to the interferogram of the transmitted wavefront; however, the gradient in the corner proved to be too steep to be removed in this way, which affects the PSF.

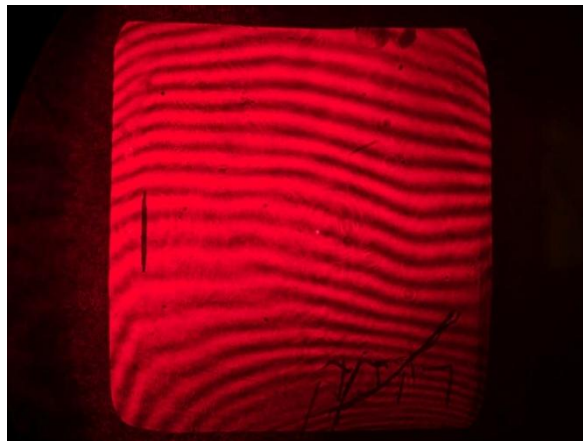


Figure 5: Interferogram of the prism in transmission (double pass). The Shack-Cube interferometer was set up with the same angle as we use the prism in CHIRON, under which the prism aperture looks nearly square. The height is 160 mm.

1.2 Fiber feed

The fiber used to feed CHIRON is a 20-m octagonal fiber from CeramOptec. Its core is 100 microns from flat side to flat side, while the cladding is circular and has a 660-micron diameter. The fiber is FC-connectorized. The fiber has low focal ratio degradation (FRD) and good transmission (see Figure 6). At F/5, 75% of the incoming energy stays encircled within an F/5 beam (that includes 86% for transmission only).

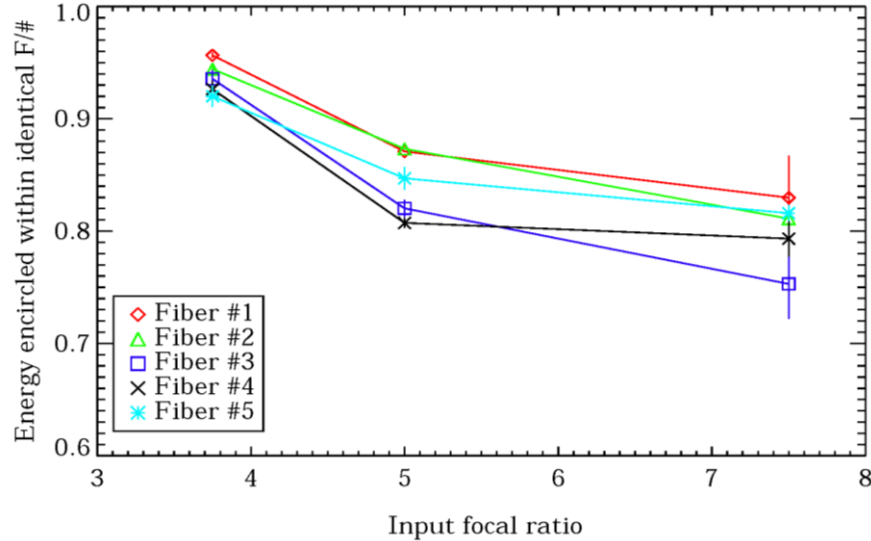


Fig 6: The focal ratio degradation of our set of octagonal fibers.

We measured the scrambling of the fiber (and four spare fibers) in May 2012. For all measurements, we used a green He-Ne laser (543 nm) and we set the input focal ratio to F/5. The light was sent into a 50 μm multi-mode fiber (object fiber). The end of the object fiber was re-imaged onto the test fiber using two achromatic lenses of focal lengths 100 mm and 75 mm respectively. The image of the object fiber is therefore 37.5 μm in diameter, while the test fibers all had a core diameter of 100 μm . This would correspond to 1 arcsecond seeing on a 2.7 arcsecond fiber, which is typical of the conditions on the 1.5 m. For realistic conditions, we incorporated a central obstruction similar to the one formed by the secondary mirror of the 1.5 m telescope.

To accurately position the spot onto the test fiber, the fiber was mounted on a precise (to less than 1 μm) translation stage with differential screws. The translation stage allows us to move the fiber with respect to the incoming beam and therefore simulate guiding errors. We imaged the spot and the front surface of the test fiber onto a camera using a pellicle beam splitter and a 300 mm lens in order to check the spot position on the test fiber.

Light from the test fiber was then collimated and re-focused onto a CCD. An additional lens moves in and out of the light path to enable measurements of the near-field (out) and the far-field (in) patterns.

In Figure 7, we see the near-field and far-field intensity patterns as a function of spot position for all octagonal fibers. The fibers were agitated in the lab to eliminate the speckle pattern. We see that compared to the round fibers, the octagonal fibers have very stable near-field and far-field distributions quasi-independent of spot position and therefore of guiding errors.

In CHIRON, a lens transforms the F/5 beam coming from the octagonal fiber into a slow focus where a slit mask and an image slicer can be moved in and out to choose the mode of operation. The slicer is a modified Bowen-Walraven image slicer that makes use of mirrors instead of prisms. It slices the fiber image into three slices of equal width, therefore tripling the resolution while minimizing light losses. The overall throughput of the slicer is 80%. Figure 8 depicts a 3D model of the slicer assembly.

Alternatively, a slit mask is attached onto the slicer assembly to provide higher resolutions: the normal slit gives $R=90,000$ while a narrow slit can increase the resolution to 120,000. The throughput of the two slits is 26% and 12%, respectively.

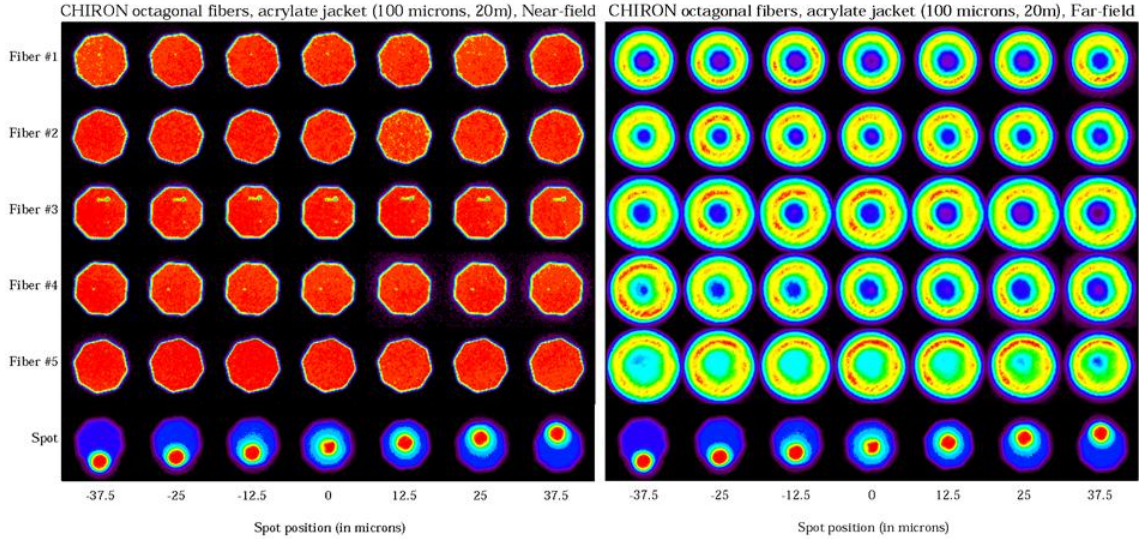


Figure 7: Near- and far field intensity patterns for the octagonal fibers we use in CHIRON, as function of the spot position.

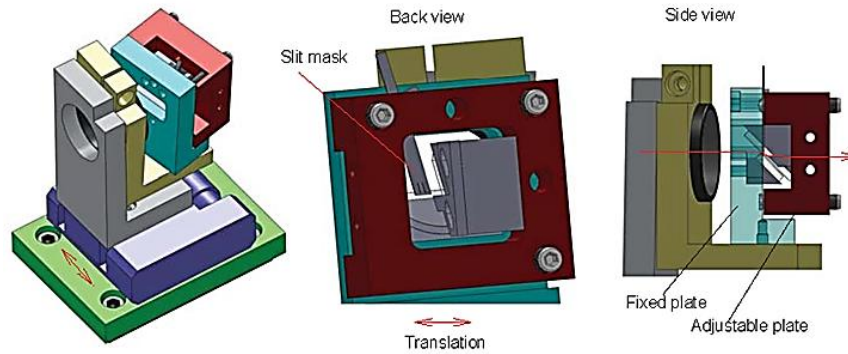


Figure 8: 3D drawings of the image slicer assembly on its translations stage.

1.3 Optical efficiency

The throughput of the bench-mounted spectrograph is excellent, because we used few optical elements and implemented optimal coatings. The two dispersive elements, the Echelle grating and the cross-dispersing prism, are of particular importance.

As noted above, the original Echelle grating in CHIRON was replaced with a new Newport grating with 31.6 g/mm and a blaze angle of 63.9 degrees (R2) during the upgrade in January 2012. The grating is coated with an enhanced silver coating, and replicated from master MR152. The measured peak efficiency is 83%, in excellent agreement with the catalog data. This is to our knowledge the most efficient Echelle grating in the Newport catalog. To allow for the installation of the vacuum chamber during the replacement work, a grating with a ruled area of 130 x 260 mm² was purchased. As the aspect ratio of the grating does not exactly match the aspect ratio of the beam at the Littrow angle, we suffer from an additional vignetting of 2%. This was deemed a reasonable compromise for being able to use a stock size grating. Further, the vacuum window introduces four glass to air interfaces into the beam. Nevertheless, the efficiency of the grating assembly improves over the original Echelle, from 55% to 79% at 550nm.

The second dispersive element is the large, single prism cross-disperser made from Schott LF7 glass, with a base length of 285 mm. The internal transmission over the full wavelength range is very good, higher than 98%, averaged over the full beam diameter.

We coated the vacuum window and the prism ourselves using the SolGel method [7]. As the substrates are irregularly shaped, we dip-coated the optics to apply a single, quarter-wave layer of silica SolGel instead of using the more common spin coating techniques for SolGel.

The other optics on the main bench are also optimized:

- The collimator and the large folding mirror use custom, enhanced silver coatings.
- The small optics are coated with commercial broad band anti-reflection (BBAR) and enhanced silver coatings.
- The camera lens is an oil-spaced triplet with BBAR coated air-glass surfaces. The two-element field flattener is BBAR coated, as well.
- The CCD dewar window, a fused silica substrate, is currently coated with a single-layer MgF_2 coating. The resulting $>1.3\%$ reflection per side are problematic so close to the detector because of ghosts. We have obtained a replacement substrate with a custom made AR coating tailored to our wavelength range, with an emphasis on the iodine region. The transmission of the Dewar window is above 98.5% over the whole spectral range; the average transmission over the full range is 99.3% and in the Iodine range it is 99.6% (Figure 9).
- Vignetting on the camera lens and the grating, as well as losses on the central obstruction of our Newton-like collimator assembly, amounts to 16%. We considered this to be a reasonable compromise between efficiency and more complicated and costly optics.

The total efficiency of the spectrograph bench was estimated by coupling using the calibration quartz lamp to feed the fiber and measuring the transmission for an 85 nm bandpass centered on 545 nm from after L1 to before the field flattener. The transmission is 60% when using the fiber mode, and 52% when using the image slicer. The optics which are not accounted for – L1, field flattener and dewar window – add only little losses of less than 4% total.

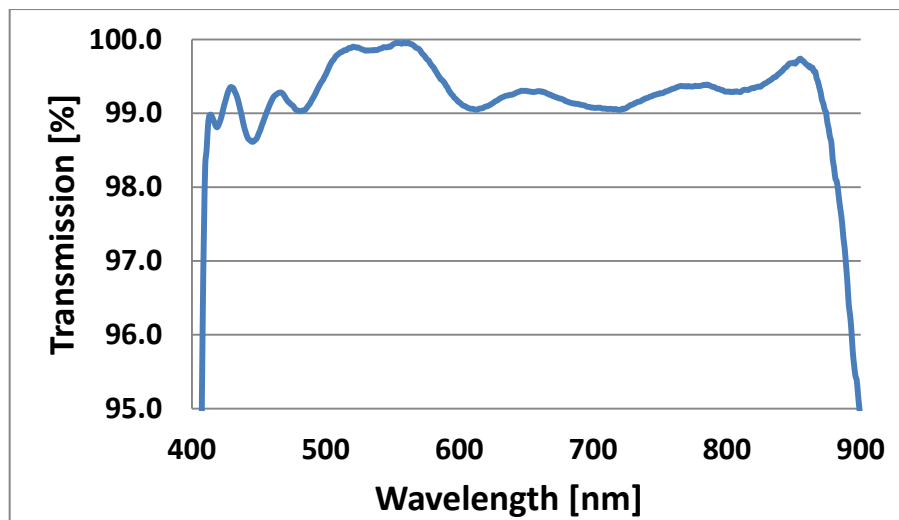


Fig. 9: The dewar window coating. The plot shows the measured transmission through the whole substrate, both sides custom AR coated. Courtesy of Chroma Technology Corp.

4. CCD AND EXPOSURE METER

4.1 CCD noise and linearity

The CHIRON detector is a CCD device CCD231-84 from e2v, with 4096x4112 square pixels of 15 μm size. It has a gradient coating in the line direction for optimum sensitivity in a wide spectral range. For this reason we orient the main (Echelle) dispersion along the CCD columns, the cross-dispersion along the lines. The CCD is housed in a dewar with liquid nitrogen cooling and a nominal holding time of 36 hours.

After CHIRON commissioning in 2011, the detector was controlled with the NOAO Monsoon Orange controller and exhibited 1.5% non-linearity. The detector read out in 60 seconds with a single amplifier in fast readout mode. As part of the upgrade, P. Moore installed a new Torrent controller developed at NOAO [8]. The controller is connected to the

dewar by two short 40 cm cables. We do not see any measureable nonlinearity at 90% of full well capacity. To our knowledge, CHIRON is the first astronomical instrument using the Torrent controller.

The Torrent controller works in the “normal” readout mode with a pixel rate of 129 kHz. Readout of full un-binned chip with 4 amplifiers takes 28 s. We normally use the CCD with 3x1 or 4x4 binning which shortens the readout time to 18 s and 5 s, respectively. The gain is about 1.3 electrons per ADU. The readout noise of 5.4 to 5.7 electrons in this mode is higher than the intrinsic CCD noise, being affected by a periodic component which shows as “fringes” in the bias frames that originate in the controller. The fast readout mode is available, but not used because of higher readout noise (10-12 electrons) and worse linearity.

Linear response of the CCD is important for precise spectroscopy. In this respect, our CCD+controller combination is excellent in the full signal range up to 65 kADU. We measured the response by exposing the CCD to a diffuse light from an LED installed inside CHIRON and driven by the shutter signal with stabilized current. The ratio of counts to exposure time is constant to 0.5% or better. We developed an alternative method to investigate gain and linearity from the ratio of two images (e.g. quartz lamp spectra). This method does not require flux stability and can be applied to calibration spectra at any time. Its results are consistent with the traditional method of CCD characterization.

The charge transfer efficiency (CTE) is yet another critical parameter for precise RV. It is excellent in both line and column directions; we can only place only upper limits on the charge spread: less than 10^{-5} per transfer.

4.2 Overall instrument efficiency

To measure the total efficiency of CHIRON (the ratio of recorded flux to the stellar flux outside the atmosphere), we used the spectral flux density outside atmosphere for a $V = 0$ star of type A0 as tabulated in [9]. The spectral flux in $\text{erg}/(\text{cm}^2 \text{ s } \text{\AA})$ is listed there. Its logarithm is a smooth function of the wavelength λ in Angstrom, well represented by a quadratic polynomial:

$$\log_{10} F_{\lambda} \approx -6.6884 + (-4.125 \times 10^{-4})\lambda + (1.70 \times 10^{-8})\lambda^2$$

This polynomial differs from the tabulated values by no more than 0.01 and gives correct flux for the $V = 0$ and $B = 0$ stars also listed by Allen ($\log_{10} F_{\lambda}$ of -8.43 and -8.17 , respectively). On June 5 2012, we observed three bright A stars several times with little airmass and in good conditions. The stars are listed in Table 1.

Table 1: Standard stars used to determine the total throughput of the instrument, and the airmass values during the observations.

Star	Type	B	V	Airmass
HR4802	A2V	3.907	3.852	1.071
HR4933	A0V	4.857	4.830	1.070
HR5881	A0V	3.529	3.549	1.311

The spectra were extracted using our regular pipeline. Flux near the blaze peak in each order is averaged over 40-pixel swath, compared to the flux outside atmosphere calculated from the V magnitude, and used to compute the efficiency $e(\lambda)$. The telescope diameter is 1.5m with a central obstruction of 0.507. The pixel scale in each order in \AA is determined from the wavelength solution in the reduced spectra. Figure 10 gives a representative efficiency curve. The dip around 7600 \AA is caused by atmospheric absorption; other dips are produced by Balmer lines that happen to be near the blaze peak. We found a peak efficiency of 7.3%, but more typically of 6% for different observations.

Surprisingly, this is about a factor of 2 lower than our expectations, assuming standard models for atmospheric transmission, the fiber throughput measured in our lab, and conservative numbers for the mirror coatings of the telescope itself. While investigating short exposure time series of Alpha Cen A and B, we found that the throughput is highly variable on short time scales, with peaks a factor of two higher than the average efficiency. We suspect the dominant losses stem from the poor guiding performance of the old tracking system, explaining the discrepancy between the theoretical throughput calculated by multiplying the values we measured for the components separately, and the actual efficiency measured on sky.

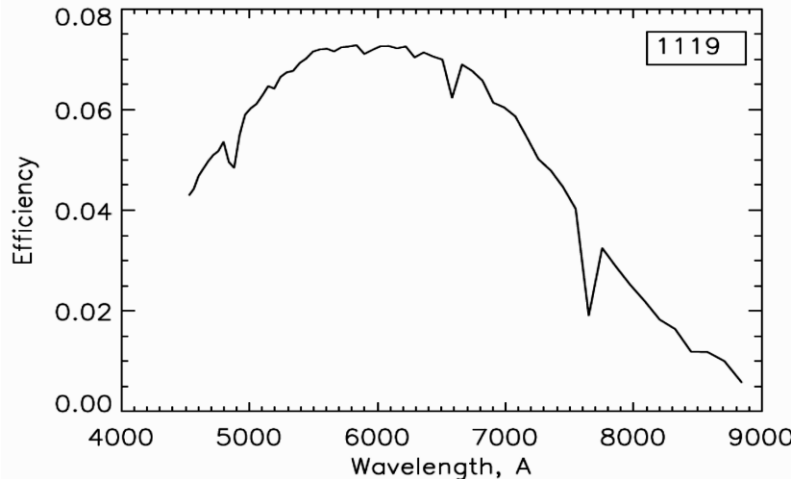


Fig 10: Absolute total efficiency of CHIRON as measured by observations of HR4933.

4.3 Exposure meter

The exposure meter (EM) system serves two purposes. First, it terminates the exposure when the desired counts have been acquired. This function keeps the exposures from being saturated during times when the seeing/telescope are operating at high efficiency and extends the exposure time in order to acquire good SNR spectra during the other times. The second function is to calculate the photon-weighted mean time of each exposure, so that the appropriate correction for the barycentric motion can be made. This is critical for precise radial velocity measurements when the photon flux changes because of guiding errors or variable cloud cover.

The optical system of the exposure meter is fairly simple. A small mirror directs a fraction (1%) of the light from the collimated beam into an optical fiber that takes that light to a photomultiplier tube. The mirror is wedge-shaped, and is mounted radially along the direction of one of the legs holding the optics that deliver the beam from the fore-optics box to the collimation mirror. The beam is focused onto the end of a 200 micron optical fiber. The other end of the fiber goes into an enclosure that holds a filter to define the bandpass of the exposure meter (currently 80 nm centered at 545 nm to match the peak of the iodine region), and a Hamamatsu H9319-11 PMT. The digital output from the PMT goes to the serial port of a dedicated computer running Linux. A copy of the signal that commands the shutter in CHIRON is passed to a circuit and connected to the parallel port of this computer.

The software is constructed as several programs using UNIX sockets for client-server communications. This separation serves to insulate the main driver, which is always monitoring the signal from the PMT for inadvertent bright light exposure, which could damage the device. This main server monitors the parallel port driver and the serial port. One client receives the string of binned samples from the main server, and sends the control software the requests to close the shutter when the signal threshold is going to be achieved. The second client receives the results of the calculation of the photon-weighted mean time, and sends these to the CHIRON control program for inclusion in the FITS headers of the image. The CHIRON control program also makes connections to these modules - one to get status and to provide for manual control of the PMT high voltage, one to display plots of the current light levels, and another to change the threshold for the function that terminates the exposures when the desired signal levels have been obtained.

5. STABILIZATION OF TEMPERATURE AND PRESSURE

5.1 Pressure monitoring

The CHIRON bench is mounted inside a metal enclosure. The enclosure is constructed from steel profiles and sheet metal which was attached with screws and silicone glue at the edges. The lid is sealed with foam to prevent dust from entering the spectrograph, but the enclosure is not tight enough to decouple the spectrograph from outside pressure changes. We attempted to slightly over-pressurize the enclosure, but the leak rate was too high for this to be useful. During the second commissioning, we installed a high precision barometer, a Weston Aerospace Model 7851AA; the pressure inside CHIRON is continuously logged. Figure 11 shows the recorded pressure variations over one week. Diurnal drifts and other short time scales are apparent.

At the altitude of the observatory, the mean atmospheric pressure is approximately 780 mbar. We observe a maximal variation of ambient pressure of about 9 mbar, which changes the refractive index of air by approximately 2.42×10^{-6} . This leads to a change in optical path length of the grating grooves, and subsequently to a calculated shift of the spectrum of 727 m/s. The pressure transducer has a resolution of <20 ppm of its full scale pressure, and can detect pressure changes that are equivalent to a Doppler shift of 2 m/s.

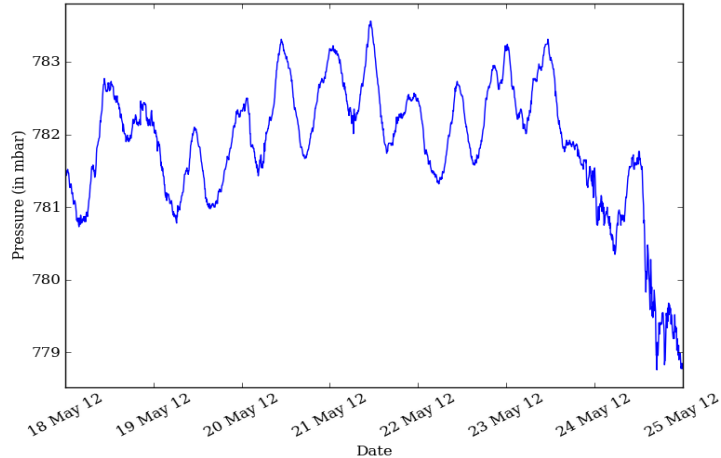


Fig. 11: The pressure inside CHIRON over the course of 7 days in May 2012.

5.2 Vacuum grating enclosure

To further stabilize the spectrum, we installed the vacuum tank and a replacement grating in January 2012. The original grating was an old R2 grating which was oversized and had $200 \times 400 \text{ mm}^2$ ruled area, on a Zerodur substrate. The peak efficiency was around 55% in the green. We replaced the grating assembly with a new grating of only $135 \times 265 \times 45 \text{ mm}^3$ size. The additional space made it possible to mount the new grating in a vacuum enclosure with the same mechanical interface as the old grating assembly, to allow for a drop in replacement. The vacuum enclosure was built in the workshops at Yale University and is made from Aluminum (6061) and stainless steel. Apart from the stainless steel flange for pumping, no welds were used, and the lids are sealed with Viton O-rings. The assembly comprises the main body, the grating cell, the back lid, valve interface, window interface, window bezel and bezel lid. The window is protected by Teflon O-rings outside the Viton O-ring and in the front.

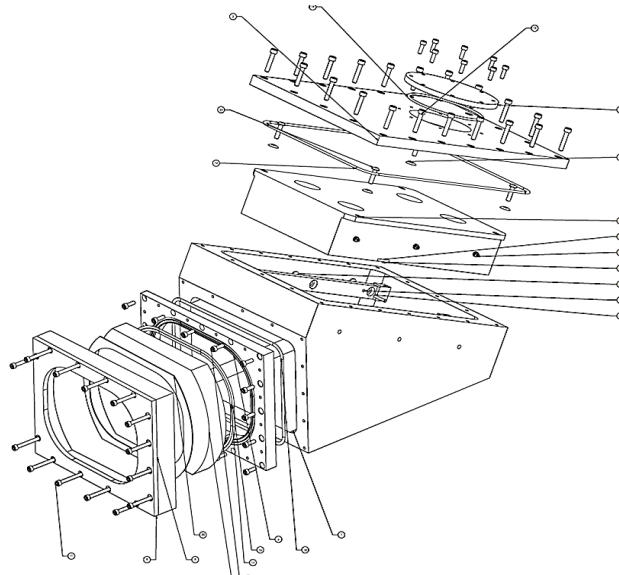


Fig. 12: Exploded view of the vacuum enclosure for the Echelle grating. The wedged window is mounted on the left, the grating is inserted in an internal cell, visible at the top right, with four holes on the back.

The vacuum window is made from a 210mm diameter Schott BK7 substrate, 25 mm thick. It is wedged in the cross dispersion direction (parallel to the optical table) with an angle of 1.5 degrees. Furthermore, the vacuum side of the window is tilted in the same direction with an angle of 1.5 degrees to the surface normal of the grating. This was designed to locate the ghosts (single and double reflection) outside the field of view of the CCD. However, as the sensitivity of the CCD extends well beyond the range of the spectrograph, we see the infrared tail of the direct ghosts. The ghosts enter the CCD on the blue side of the Echelle format; fortunately falling outside the FSR of the affected orders so that it was not necessary to replace the window interface plate.

The vacuum window of the grating is coated with a single layer of silica SolGel, with a reflectivity minimum at 550nm for the nominal 6 degrees incidence angle. We used a green HeNe laser to measure a reflectivity of <0.25% per surface.

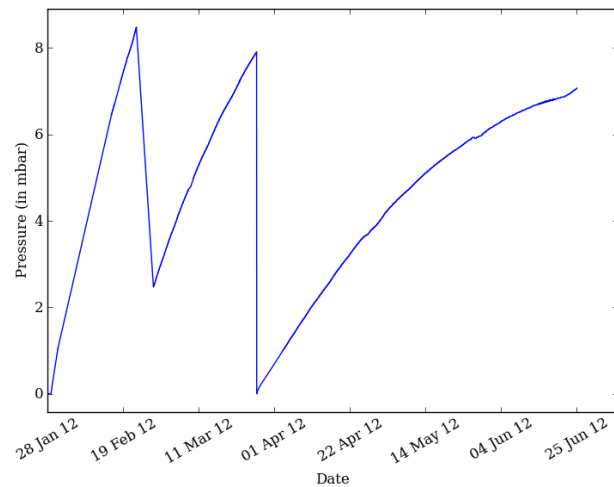


Fig. 13: The pressure inside the Echelle vacuum enclosure. The chamber was pumped for the first time on Jan. 28, and due to outgassing re-pumped 4 and 8 weeks later. We allow for a maximal pressure of 8 mbar, 1% of the ambient pressure. The current hold time is > 3 month, and we expect this value to get better after the next pumping cycle. The small dips at the end of April and end of May coincide with temperature drops due to work on the temperature controller.

The replacement grating is mounted in a grating cell and held by three hard points laterally and axially. The axial hard points are formed by flat stainless steel clamps, which are 20 mm long and intrude 2 mm into the grating surface. Between the steel and the grating we use a thin sheet of Teflon to minimize friction. Laterally, the hard points are formed by ball screws. We use spring loaded screws opposite the hard points in all directions to preload the mount.

The old grating assembly suffered from a slight astigmatism, introduced by deformation under gravity. We investigated three possible mounting options for the new grating to overcome this problem. The first is to mount the grating with invar pads glued onto the back of the substrate. This allows supporting the grating at a better position on the surface rather than on the edge. Laiterman et al. [10] derived a procedure to reliably glue invar pads to Zerodur. Unfortunately, this option is mechanically complicated and the gluing poses a risk for the grating. The second option is to invert the grating and mount it facing upwards. As it is enclosed in a vacuum chamber, this does not impact dust contamination issues etc. Kinematically, this option seemed ideal; however, it would have led to a different orientation of the elliptical footprint of the beam on the prism aperture compared to the situation before the upgrade. We adopted a third option, mounting the grating face down on three small pads, similar to the configuration for the original grating. As the new substrate is much smaller, the astigmatism is reduced. We ran different finite element models to test where to position the pads. Figure 14 shows the acceptable low surface sag in a crosscut through the center of the grating along the long axis, for different locations of the mounting pads. One mounting pad was always located at the bottom of the grating in the center of the short edge; the other two mounting pads were located symmetrically on the left and right long edge at different distances from the bottom. The minimal deviation was found when the pads were located about 20% from the end of the substrate. However, a tilt of the surface can be compensated by realigning the beta angle of the mount; we found that a pad position of 33% yields better results. If a linear fit to the deflection curve is subtracted, effectively removing a tilt, the residual deformation is only 20 nm peak to valley. This mounting option had the least impact on the rest of the spectrograph.

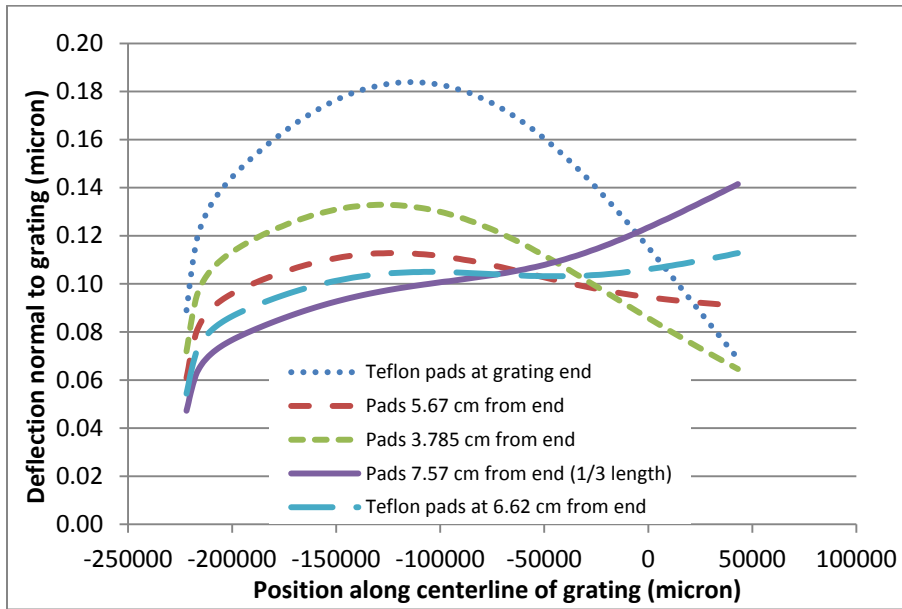


Figure 14: Finite Elements model of the surface sag of the grating substrate evaluated at a crosscut through the center. The substrate was held on three pads on the edge of the surface, one at the bottom of the grating, and two at various positions on the sides. As tilt can be removed, the solid line, corresponding to a pad position located at $2/3^{\text{rd}}$ of the length of the substrate yields the best result.

The movement of the spectrum on the detector due to temperature and pressure changes is about three orders of magnitude higher than our desired Doppler precision. In addition to translation of the spectrum, pressure changes induce variability in the dispersion. In principle, the iodine technique allows us to model and track these changes in the spectrum. However, imperfect modeling of spurious movement of the spectrum is a likely source of systematic errors that we would like to eliminate.

The spectral dispersion is dependent on the groove spacing and the pressure of the medium in which the grating is immersed. In Figure 15 we compare the variation in dispersion with and without the vacuum enclosure installed around the grating. The plot shows the standard deviation of the dispersion measured in a 40 Angstrom segment of the spectrum for a series of spectra taken during the course of one night, with and without the vacuum enclosure in place. The variability in dispersion throughout the night is reduced by almost a factor of four with the vacuum enclosure.

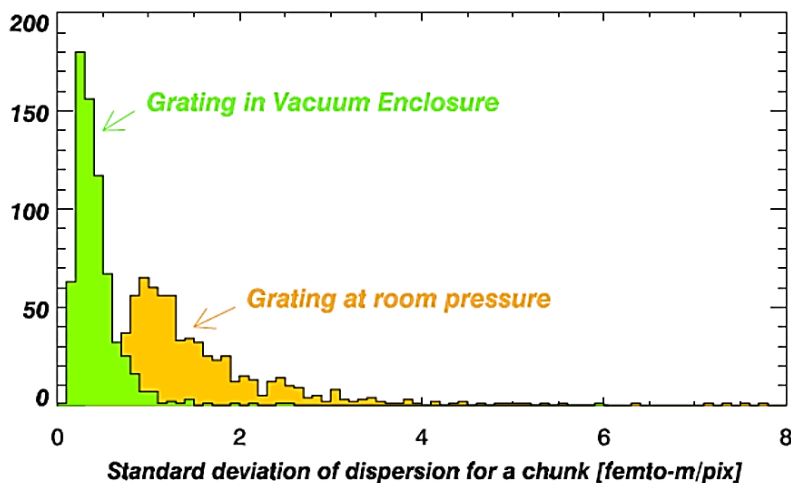


Fig 15: Histogram of the standard deviation of the dispersion with and without the vacuum enclosure.

5.3 Temperature stabilization

Accurate stabilization of the instrument temperature is required to minimize displacement of the spectrum on the detector caused by temperature-related mechanical deformations and by the thermal expansion of the grating, which affects its groove spacing despite the low CTE of Zerodur. The temperature is controlled by two loops: internal, acting on a heater inside the instrument, and external, stabilizing the air around CHIRON.

During the upgrade in 2012, a “warm room” was assembled around CHIRON (Figure 16). It consists of an aluminum frame made of 80/20 truss and a flexible insulation material, PRODEX polyethylene foam covered by aluminum foil on both sides. The insulation can easily be removed to access CHIRON when needed, i.e. for pumping the Echelle enclosure. In addition, the ceiling of the warm room is covered from outside by 5 cm Styrofoam panels to reduce the heat loss. Air inside this room is maintained at constant temperature of +20°C by the combination of 400 W oil-filled heater, sensor, and control unit. To prevent thermal stratification gradients, three fans force air circulation. One fan circulates cooler air from the floor toward the heater; another fan located near the ceiling blows downwards and the third fan under CHIRON (which is elevated by 0.2 m above the floor) also blows towards the heater.

The room temperature controller is based on commercial components from Omega: the standard analog-output controller CNi852-C24x and the silicon-controlled rectifier SCR19Z-12-040. The SCR regulates current in the 110V heater by switching it on or off at crossings of the line voltage, thus reducing potential electrical interference. It can output up to 40A current, much more than actually needed. An RTD 100 platinum sensor suspended inside the warm room at ~1 m above the floor provides the signal for standard proportional-integral feedback. Another sensor monitors the air temperature independently at a different location inside the room.

The optical elements of CHIRON are mounted on a vibration dampened optical table which is attached to the support structure semi-kinematically at 3 points. This structure also acts as instrument enclosure. It is insulated from the outside by 25 mm thick rigid foam panel made from polyisocyanurate. Three heating elements are glued to the support structure below the table. The table is isolated from below by foam, preventing direct heating. The temperature is monitored inside of the spectrograph enclosure by four RTD sensors.

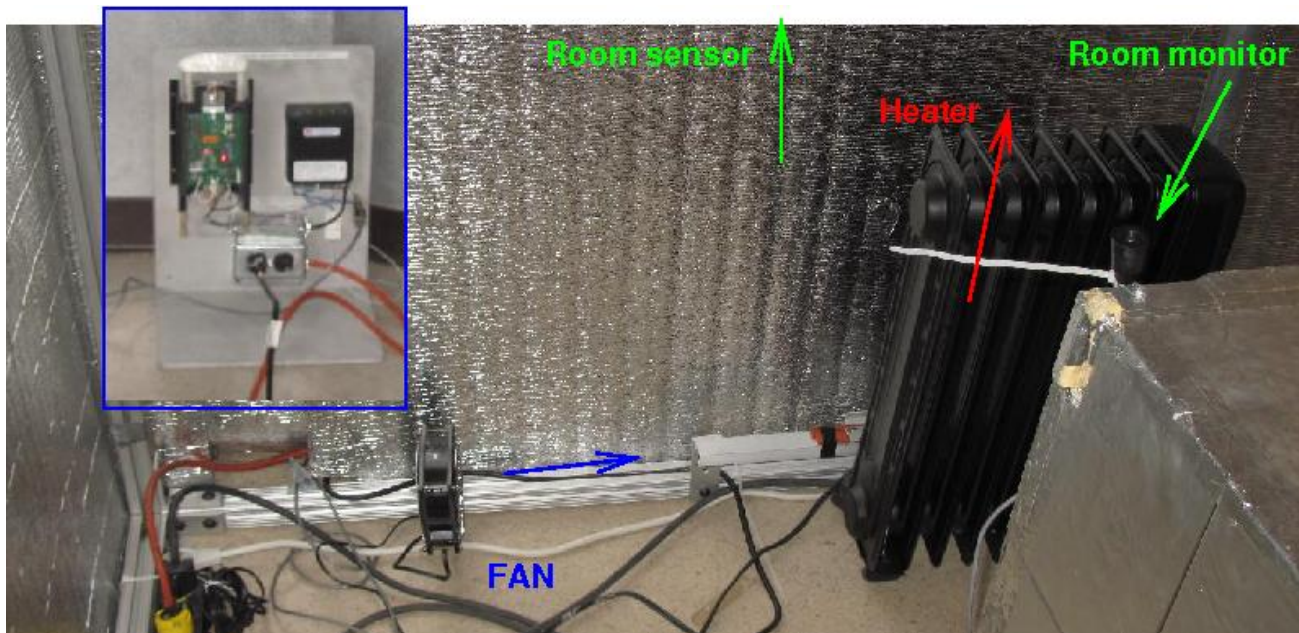


Fig. 16: Inside the shiny warm room. The corner of spectrometer is seen in the lower right; some elements of the air temperature control are indicated. The insert shows the controller located outside the warm room

In the first year of operation, we controlled CHIRON temperature with an Omega unit, accurate only to 0.5°C. During the upgrade, this unit was replaced by the much more accurate Lakeshore Model 325 device. The internal heater produces a maximum of 100W power at 110V, and is now driven by the Lakeshore low-voltage output. Now that

CHIRON operates in the temperature-controlled environment, no more than 12.5W are needed to maintain the instrument at +21°C, slightly above ambient temperature. Small power means small heat flux and small temperature gradients inside the instrument. In fact CHIRON uses less than 50% of the heater power in normal operation, a mere few Watts!

The CCD Dewar is attached to the support structure, rather than the optical table to de-couple perturbations (variable mass and temperature) from the optical train. For the same reason the dewar and its controller, which outputs 35 W of heat into the air, are outside the thermal enclosure. However, the thermal resistance between the dewar and the structure is not high enough, so there is some heat flux from internal heater to the dewar; this flux depends on the temperature of the un-stabilized air outside the warm room. We continue to work on fine-tuning these aspects of the temperature control.

Figure 17 plots temperature logs for one week with stable temperature control. The air in the warm room was maintained close to the set point with rms fluctuations of 0.05C. Spikes correspond to people entering the Coude room for daily refills of the dewar. The rms variation of temperature inside CHIRON was only 0.015C. There is a constant systematic difference between these points indicative of a heat flux (grating is the coldest, as it is further from the heater). Moreover, the temperatures are all above the +21C set-point, while the sensor is, of course, maintained at +21C with a high accuracy; it is rather close to the dewar attachment place. There was no such difference when the system operated without the dewar in the test phase. We plan to correct this in the near future.

The iodine cell is located inside the spectrometer and is maintained at +40C. It is placed inside small aluminum box heated by a 1.2 kOhm/10W resistor driven by another Omega controller. The box is insulated with foam and consumes only 1-2W of power. This is a heat source inside CHIRON, but only a small and constant one.

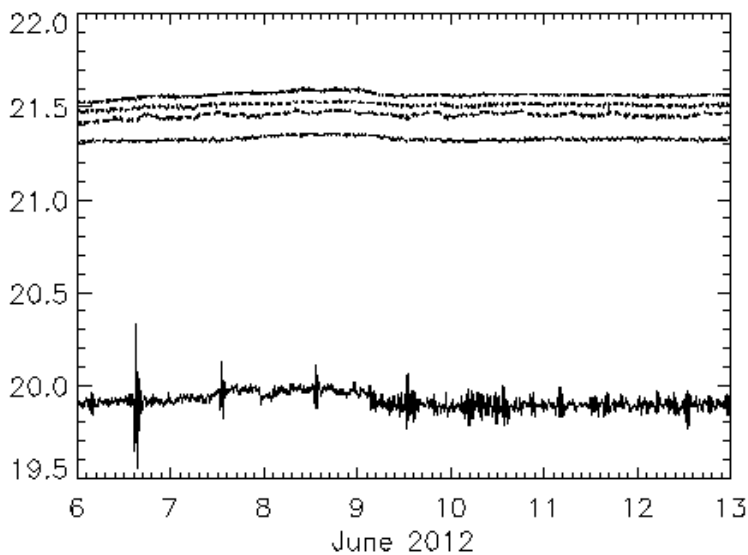


Fig. 17: Temperature record during one week in June 2012. The lower curve is warm-room temperature, the next higher curve is the grating, and the three upper curves are temperatures at monitoring points inside CHIRON.

6. CHIRON STABILITY AND RV PRECISION

6.1 Spectrum stability

We used calibration exposures taken with a Thorium Argon lamp with different temperatures inside CHIRON to assess the sensitivity of the position of the spectra to temperature changes. To measure the change in position, we cross-correlated the first frame in the dataset with all subsequent frames, and plotted the shift in dispersion direction as well as in cross dispersion direction (Fig. 18). In dispersion direction we find a shift of about 4.8 km/s per Kelvin.

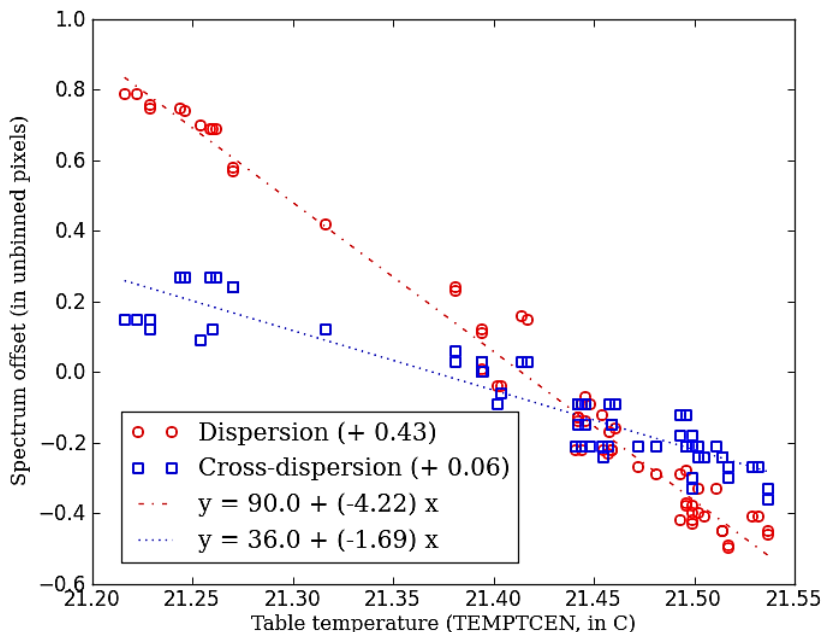


Fig. 18: spectral shift as a function of the temperature of the optical bench, measured from ThAr exposures. Circles denote the shift in dispersion direction, squares in cross dispersion direction. The slope of the linear fit to the dispersion direction data is equivalent to a RV shift of 4.8 km/s per Kelvin.

To estimate the stability of the spectrograph over timescales of minutes to hours, we ran a series of ThAr calibration exposures during daytime and used the same method of cross-correlating the spectra as for the correlation with spectral shift and temperature, above; the shift in dispersion direction is shown in Figure 19. The available dataset is too short to draw definite conclusions, and our simple cross-correlation adds noise at very small spectral shifts; however, the data indicates that one can achieve a Doppler precision better than a few tens of m/s when bracketing a science exposure with ThAr calibration frames.

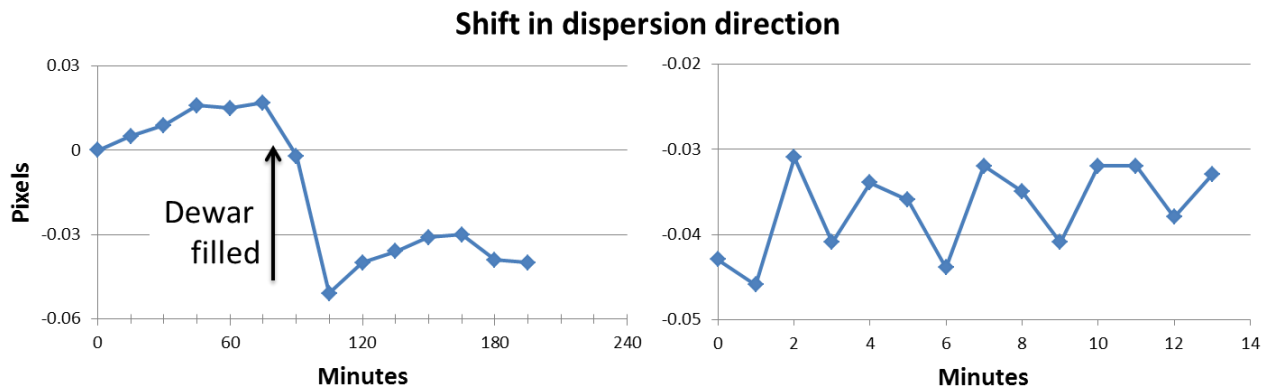


Figure 19: Spectral shift in dispersion direction determined by cross-correlating ThAr spectra over medium and short timescales. 0.01 pixel shift corresponds to 11 m/s.

6.2 Radial velocities with iodine cell

The CHIRON upgrade was completed on June 4, 2012. The exposure meter provides uniform exposures with SNR = 315 for the bright stars alpha Cen A and B, yielding a single measurement precision of 0.6 m/s. In comparison, the observations from 2011 (before the upgrade and before the exposure meter had been installed) have signal-to-noise ratios ranging between 20 and 200 with single measurement precisions of about 1.0 m/s. However, we have not carried out Doppler modeling on a long enough time baseline of data to assess the magnitude of systematic errors.

7. SUMMARY

The CHIRON spectrograph was commissioned in March 2011 as a precision radial velocity spectrometer for exoplanet searches at Cerro Tololo InterAmerican Observatory (CTIO). This spectrograph is a facility instrument with significant time available through the SMARTS consortium. The spectrograph has an automated pipeline reduction for four observing modes (fiber with $R=28,000$; slit with $R=90,000$; slicer with $R=90,000$ and narrow slit with $R=120,000$) and SMARTS users can download both raw and extracted, wavelength calibrated spectra. A small fraction of public access time is also available through the NOAO time allocation process.

CHIRON also serves an important role as a testbed for understanding how to further improve radial velocity precision. After the first six months of operations in 2011, we identified a number of upgrades to improve the stability of the instrument. In January 2012, we installed a new higher efficiency Echelle grating in a vacuum enclosure and have now demonstrated a factor of four improvement in the stability of the instrumental dispersion (Figure 15). A new NOAO Torrent controller was installed in February 2012. We applied a SolGel anti-reflection coating to the prism to improve throughput. The round 100 micron fiber was replaced with a 100 micron octagonal fiber producing a factor of five improvement in the stability of the instrumental spectral line spread function (Figure 7). An exposure meter was installed to calculate photon-weighted centroids for our exposure times and to auto-terminate the exposures when a requested SNR has been obtained. This produces uniformly exposed spectra, eliminating the factor of ten range in SNR in spectra that we obtained in 2011. We also took advantage of the down time for CHIRON to obtain a new high resolution, high SNR scan of our iodine cell with a Fourier Transform Spectrograph. The instrument is now fully upgraded and we are obtaining radial velocities with a single measurement precision of 0.6 m s^{-1} for $\text{SNR}=300$ spectra.

ACKNOWLEDGEMENTS

We thank Thomas Blake at Pacific Northwest National Laboratory for obtaining an optical FTS scan of our iodine cell. We thank David Sprayberry and Peter Moore for their work commissioning the Torrent Controller. Many thanks to Marco Bonati at CTIO, who developed the software used to control CHIRON and to acquire the spectra. We thank Jeff Valenti for help with the FTS atlas and John Brewer for his work on the automated observing scripts for CHIRON and for SMARTS users. We thank Drew Phillips and Jim Stilburn for their advice on SolGel coatings, and Jeff Crane for helpful comments on vacuum enclosures. Many thanks to the staff at the CTIO and Yale workshops for their excellent work, and to Will Emmet at Yale for his help in designing the vacuum chamber. DAF acknowledges grant support from NSF AST-1109727 and NASA NNX12AC01G and support from Yale University that enabled the CHIRON upgrades. DAF and JFPS acknowledge support for optimizing fiber scrambling from the Planetary Society.

REFERENCES

- [1] Raskin, G., Van Winckel, H., Hensberge, H. et al. "HERMES: a high-resolution fibre-fed spectrograph for the Mercator telescope," *A&A*, 526, 69 (2011).
- [2] Perruchot, S., Kohler, D., Bouchy, F. et al. "The SOPHIE spectrograph: design and technical key-points for high throughput and high stability," *Proc. SPIE*, 7014, 17 (2008).
- [3] Pepe, F., Mayor, M., Delabre, B. et al. "HARPS: a new high-resolution spectrograph for the search of extrasolar planets," *Proc. SPIE*, 4008, 582 (2000).
- [4] Crane, J. D., Shectman, S. A., Butler, R. P. et al. "The Carnegie Planet Finder Spectrograph: integration and commissioning," *Proc. SPIE*, 7735, 170 (2010).
- [5] Pepe, F. A., Cristiani, S., Rebolo Lopez, R. et al. "ESPRESSO: the Echelle spectrograph for rocky exoplanets and stable spectroscopic observations," *Proc. SPIE*, 7735, 14 (2010).
- [6] Schwab, C., Spronck, J. F. P., Tokovinin, A., Fischer, D. A. "Design of the CHIRON high-resolution spectrometer at CTIO," *Proc. SPIE*, 7735, 149 (2010).
- [7] Huntten, M.; Buchholz, N.; George, R. et al. "New developments for detector controllers at NOAO," *Proc. SPIE*, 7742, 53 (2010).
- [8] Cox, A. N., [Allen's astrophysical quantities], New York: AIP Press; Springer, (2000).
- [9] Laiterman, L. H., Radovan, M. V., Cabak, G. F., "Experimental investigation of adhesive bond strength between metal and optical glass," *Proc. SPIE*, Vol. 7735, 135 (2010).
- [10] Phillips, A. C., Miller, J., Brown, W., et al., "Progress toward high-performance reflective and anti-reflection coatings for astronomical optics," *Proc. SPIE* 7018, 70185A (2008).